frontiers | Frontiers in Physics

BRIEF RESEARCH REPORT
published: 24 June 2022
doi: 10.3389/fphy.2022.897255

Active Condensation of Filaments Under Spatial Confinement

Saad Ansari[1]*, *Wen Yan*[2], *Adam Ray Lamson*[2], *Michael J. Shelley*[2,3], *Matthew A. Glaser*[1,2] *and Meredith D. Betterton*[1,2,4]

[1]Department of Physics, University of Colorado Boulder, Boulder, CO, United States, [2]Center for Computational Biology, Flatiron Institute, New York, NY, United States, [3]Courant Institute, New York University, New York, NY, United States, [4]Department of Molecular, Cellular, and Developmental Biology, University of Colorado Boulder, Boulder, CO, United States

Living systems exhibit self-organization, a phenomenon that enables organisms to perform functions essential for life. The interior of living cells is a crowded environment in which the self-assembly of cytoskeletal networks is spatially constrained by membranes and organelles. Cytoskeletal filaments undergo active condensation in the presence of crosslinking motor proteins. In past studies, confinement has been shown to alter the morphology of active condensates. Here, we perform simulations to explore systems of filaments and crosslinking motors in a variety of confining geometries. We simulate spatial confinement imposed by hard spherical, cylindrical, and planar boundaries. These systems exhibit non-equilibrium condensation behavior where crosslinking motors condense a fraction of the overall filament population, leading to coexistence of vapor and condensed states. We find that the confinement lengthscale modifies the dynamics and condensate morphology. With end-pausing crosslinking motors, filaments self-organize into half asters and fully-symmetric asters under spherical confinement, polarity-sorted bilayers and bottle-brush-like states under cylindrical confinement, and flattened asters under planar confinement. The number of crosslinking motors controls the size and shape of condensates, with flattened asters becoming hollow and ring-like for larger motor number. End pausing plays a key role affecting condensate morphology: systems with end-pausing motors evolve into aster-like condensates while those with non-end-pausing crosslinking motor proteins evolve into disordered clusters and polarity-sorted bundles.

Keywords: active matter, filaments, microtubules, self-organization, confinement, crosslinking motors, condensation

OPEN ACCESS

Edited by:
Kevin Mitchell,
University of California, Merced, United States

Reviewed by:
Daniel Beller,
University of California, Merced, United States
Jennifer L. Ross,
Syracuse University, United States

****Correspondence:***
Saad Ansari
saad.ansari@colorado.edu

Specialty section:
This article was submitted to Soft Matter Physics, a section of the journal Frontiers in Physics

Received: *15 March 2022*
Accepted: *01 June 2022*
Published: *24 June 2022*

Citation:
Ansari S, Yan W, Lamson AR, Shelley MJ, Glaser MA and Betterton MD (2022) Active Condensation of Filaments Under Spatial Confinement. Front. Phys. 10:897255. doi: 10.3389/fphy.2022.897255

1 INTRODUCTION

Active matter is composed of energy-consuming units that generate activity through motility. Emergent behavior, like global contraction, collective motion, and turbulent flow underpin active matter systems [1–4]. Self-organization in active matter can form structures orders of magnitude larger than the size of a single particle [5–7]. Systems of attractively interacting colloidal particles exhibit phase coexistence, where a low-density vapor state surrounds a denser liquid, gel, or solid state [8–10]. Cytoskeletal filaments can undergo *active condensation*, by influence of transient crosslinking motors. Filaments condense into aster-like structures in the presence of end-pausing crosslinking motors [1, 7, 11, 12]. Active condensation may be considered a non-equilibrium analogue of micelle formation, where hydrophobic interactions between amphiphilic molecules lead

to phase separation [13, 14]. In active condensation of filament asters, end-pausing crosslinking motors accumulate at filament tips, producing an effective attraction between filament ends. In the case of non-end-pausing crosslinking motors, the effective crosslink-mediated attraction is distributed along filament lengths, bundling adjacent filaments [2, 3, 5]. In the absence of end-pausing, crosslinking motors walk along filaments, generating rich dynamics from both extensile and contractile stresses [11].

While the bulk behavior of filament-motor assemblies has been extensively studied, the effects of confinement on such assemblies is not well studied. Confinement is biologically important as filaments and molecular motors self-assemble within the confines of cellular membranes and in the presence of organelles. Geometric constraints introduced by boundaries, both in cells and in microfabricated chambers, influence self-organization, leading to positioning and alignment of the cytoskeletal components [15–19]. Xenopus egg extract confined within small spherical droplets forms cortical and half-aster cytoskeletal structures [20, 21]. Microtubules under confinement with non-end-pausing motors generate vortices and continuous flows [22–24]. Boundaries alter the dynamics by blocking kinetic pathways, and therefore change the morphology of condensed structures. Despite previous work, our understanding of how confinement perturbs morphology of active condensates is limited [2, 20]. Improved understanding of the interplay between crosslinking motor activity and confinement in cytoskeletal active matter gives insight into their biological functionality in living organisms.

Here, we investigate the role of confinement on the active condensation of filaments and crosslinking motor proteins using large-scale Brownian Dynamics/kinetic Monte Carlo (BD/kMC) simulations. In particular, we consider spherical, cylindrical and planar confining geometries. We find that both geometry and confinement lengthscale affect condensate morphology. In systems with end-pausing motors, aster formation is inhibited at small confinement lengthscales. Spherically-confined systems assemble into both half and full asters. Cylindrically-confined systems condense into polarity-sorted bilayers at small confinement lengthscales and bottle brush-like states at large confinement lengthscales. Systems confined between planar surfaces condense into flattened asters at small confinement lengthscales. Under planar confinement, flattened asters become hollow and ring-like when the number of crosslinking motors is increased. For end-pausing crosslinking motors that walk to filament plus ends, motor accumulation induces a highly local effective attraction between filament plus ends that is analogous to the association of head and tail groups of amphiphilic molecules seen in micelle formation. In contrast, non-end-pausing crosslinking motors induce attraction between filaments distributed along their lengths. In the case of non-end-pausing crosslinking motors, and under planar confinement, filaments condense into disordered clusters at low filament packing fractions, and polarity-sorted bundles with high orientational order at high filament packing fractions.

2 METHODS

2.1 Simulations

We use a Living ENsemble Simulator (aLENS), to simulate systems of filaments and crosslinking motors [25]. Filaments are modeled as rigid spherocylinders, with fixed length L_0 = 0.25 μm and diameter D = 0.025 μm (aspect ratio 10), sterically interacting with each other. Each filament has a plus end and a minus end. The end-to-end filament length, when accounting for the hemispherical caps at both ends, is $L = L_0 + D$ = 0.275 μm. Crosslinking motors are modeled as Hookean springs connecting two binding sites or heads. Crosslinking motors do not sterically interact with each other. Filament motion, filament collision, and motor head binding/unbinding kinetics set the characteristic time scales for the system, with the timestep determined by the shortest time scale. In every timestep, aLENS calculates crosslinking motor diffusion and stepping, crosslinking motor binding/unbinding, and filament motion, in that order.

In this system, crosslinking motors can be unbound, singly bound, or doubly bound (crosslinking). Unbound crosslinking motors undergo Brownian motion. Singly bound crosslinking motors with one head bound to a filament and one unbound head, move on filaments with velocity v_s. Doubly bound crosslinking motors have both heads bound to different filaments, and each head moves with velocity v_f. Here, v_f is the force-dependent stepping velocity that changes with the motor tether stretch [26].

The binding and unbinding of crosslinker motor heads is evaluated using a kinetic Monte Carlo algorithm that treats these as stochastic events. This algorithm satisfies detailed balance in the limit of non-walking heads. Motors are modeled explicitly, and transition between unbound, singly bound, and doubly bound states with time-independent transition rates R. State transitions are inhomogeneous Poisson processes, with the transition probability given by

$$P(\Delta t) = 1 - \exp\left(-R\Delta t + O\left(\Delta t^2\right)\right). \tag{1}$$

Filaments move due to forces from crosslinking motors, steric interactions with other filaments and boundaries, and Brownian motion. Traditional simulation methods are based on interaction potentials between filaments [27], but this can lead to numerical instability and overlaps between filaments [28]. In contrast, aLENS treats filament steric interactions as non-overlapping constraints. A complementarity constraint, with interaction force $\gamma_{col} > 0$ when the minimal distance $\Phi_{col} = 0$ (contact), and $\gamma_{col} = 0$ when $\Phi_{col} > 0$ (no contact), is used. Crosslinking forces are modeled using an equality constraint that satisfies the Hookean spring model, $\gamma_{xl} = -\kappa(l_f - l_0)$, where κ is the spring constant, l_f is the spring length, and l_0 is the spring rest length. Filament-boundary steric interactions are modeled in a similar fashion to filament-filament interactions, except that interaction forces only act on filaments. Integrating the equation of motion such that these constraints are satisfied for all possible collisions and crosslinking motors, filament positions and orientations can be evolved in time. For details on the simulation methods, we refer the reader to [25].

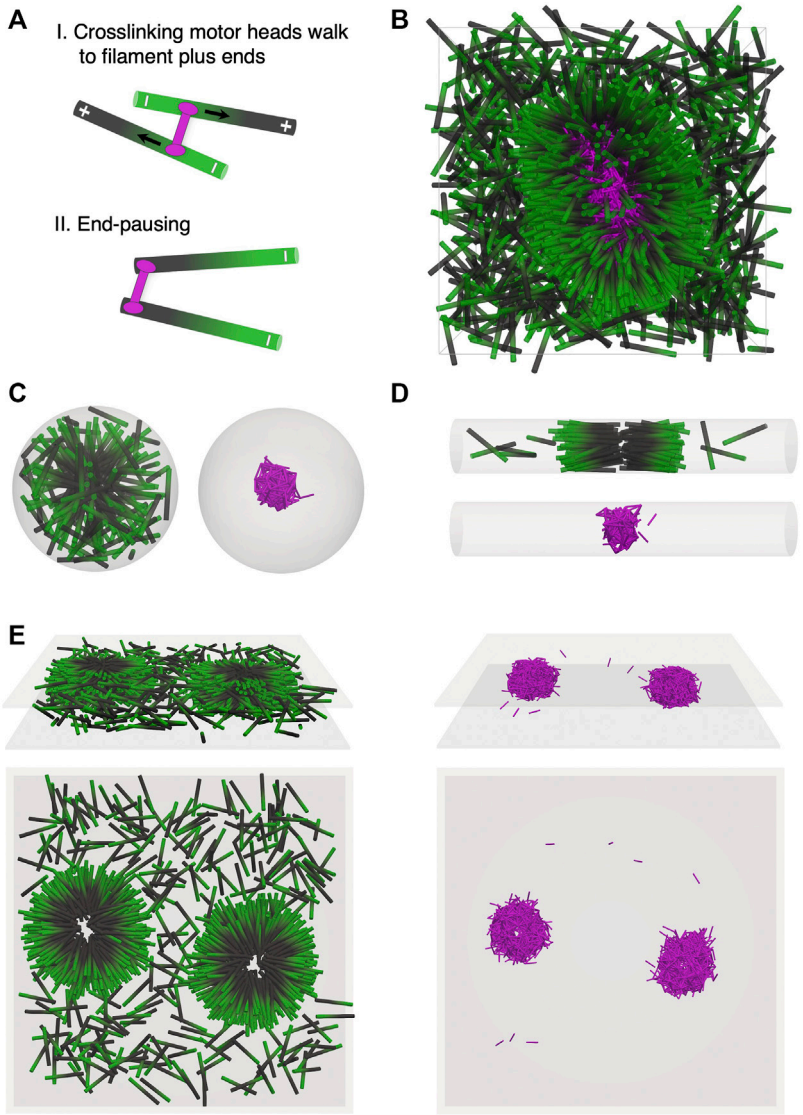

FIGURE 1 | Self-organization of filaments and crosslinking motor proteins is affected by confinement geometry. **(A)** End-pausing crosslinking motors (pink) bind to filaments (minus end green, plus end black) and each motor head walks to the plus end of the filament to which it is bound. Upon reaching the plus end, the motor heads stop walking and pause there. **(B–E)** Simulation snapshots at a filament packing fraction of $\phi = 0.08$. This corresponds to 1,600 filaments in B, D, E, and 181 filaments in C. The number of crosslinking motors in each geometry is three times the number of filaments. **(B)** Simulation snapshot of an unconfined system of filaments and crosslinking motors in a 3D periodic box. End pausing of crosslinking motor heads leads to tip accumulation of crosslinking motors on filament plus ends. **(C)** Spherical confinement. Filaments (left) self-organize into a symmetric 3D aster with the motors (right) forming a core near the center of the aster. **(D)** Cylindrical confinement. Filaments (top) form a polarity sorted bilayer oriented along the cylindrical axis. Motors (bottom) polarity sort the filaments. **(E)** Planar confinement. Filaments (left) self-organize into flattened asters due to activity of motors (right). Top (3D view) and bottom (top view).

2.2 Confinement Boundaries

In this study, we confine systems of filaments and crosslinking proteins with variable geometry. For spherical confinement, we use a sphere where spatial constraints are three dimensional. For cylindrical confinement, we use a cylinder oriented along the z-axis. As a result, spatial constraints are two dimensional in the XY plane while periodic boundary conditions are enforced along the z-axis. For planar confinement, two planes with their normal vectors oriented along the z-axis are spaced with varying separation in z. Filaments lie between the two planes and experience spatial constraints in one dimension. We enforce periodic boundary conditions along the x and y-axes. When calculating the volume of a confined system, we use the end-to-end filament length $L = 0.275$ μm instead of $L_0 = 0.25$ μm.

2.3 Initial Conditions

Filaments are initialized with an equal number oriented along the $+z$-axis and the $-z$-axis. Unless otherwise specified (as in the case of spherical confinement), our simulations contain $N = 1{,}600$ filaments. Each filament is a spherocylinder with volume $V_f = \frac{\pi D^2 L}{4} + \frac{\pi D^3}{6}$. For a

filament of length $L_0 = 0.25$ μm and diameter $D = 0.025$ μm, filament volume $V_f = 1.31 \times 10^{-4}$ μm. The filament packing fraction is defined as $\phi = NV_f/V$, where V is the system volume, and N is the total number of filaments. Crosslinking motor proteins are initialized in the unbound state, and placed at random in the simulation box. In these simulations, we vary $\tilde{N}_c = N_c/N$, the ratio of the number of crosslinking motors N_c to the number of filaments N.

3 RESULTS

3.1 Active Condensates in Confined Geometries

Filaments driven by crosslinking motor proteins can self-organize into large aggregates. We first consider plus-end-directed crosslinking motors. Motor heads that pause when they reach the filament plus end (**Figure 1A**) accumulate there. Filaments can then have a motor-rich end (the plus end in our model) and a motor-poor end (the minus end). Crosslinking produces effective attractive interactions between motor-rich filament plus ends, leading to condensation of motor-rich ends.

In **Figures 1B–E**, we show results from simulations of systems containing filaments, at packing fraction $\phi = 0.08$, and crosslinking motors. The number of crosslinking motors is equal to three times the number of filaments. Over time, motors bind to filaments, then walk and accumulate at the filament plus ends. In an unconfined system with $N = 1{,}600$ filaments and volume $V = 2.6$ μm^3, end-pausing motors drive the formation of asters (**Figure 1B**, **Supplementary Movie S1**). Filament plus ends (black) are held together by a core of crosslinking motors (pink) with the filaments oriented radially inward. A fraction of the filaments with very few motors bound to them remain in an uncondensed "vapor" state.

Confinement can alter self-organization of filaments and motors by affecting aster positioning or even preventing full aster formation. To illustrate this, we first consider a sphere of diameter $D = 3L$ and volume $V \approx 0.30$ μm^3. In this case, $N = 181$ filaments self-assemble into a spherically symmetric aster (**Figure 1C**, **Supplementary Movie S2**). When the confining boundary is a relatively narrow cylinder of diameter $D = L$, length 43.3 μm and volume $V \approx 2.6$ μm^3, filaments cannot form asters but instead condense **Figure 1D** into polarity-sorted bilayers (**Figure 1D**, **Supplementary Movie S3**). In the bilayer, filaments are aligned along the cylinder axis. Plus ends (black) are crosslinked by motors near the center of the bilayer, while minus ends are positioned on the outer edges of the condensate. For planar confinement with separation between the two surfaces $H = L$ and volume $V \approx 2.6$ μm^3, flattened asters form (**Figure 1E**, **Supplementary Movie S4**). Filament plus ends are held together by a dense core of crosslinking motors. Filaments have a tendency to lie in planes parallel to the confining surfaces (**Figure 1E**, top left view).

3.2 Confinement Lengthscale Determines Morphology

The confinement lengthscale can affect condensate morphology by preventing the formation of the symmetric asters that are favored in bulk systems. We first investigate spherical confinement with a fixed filament packing fraction of $\phi = 0.08$ for sphere diameters D in the range 1–$3L$ (**Figure 2A**). In these three cases, we simulate $N = 6$, 53, and 181 filaments in spheres with volume $V \approx 0.01$, 0.09, and 0.30 μm^3 respectively. The ratio of the number of crosslinking motors to the number of filaments is $\tilde{N}_c = 3$, so that the systems contain 18, 159, and 543 crosslinking motor proteins each. When $D = L$, spatial constraints prevent motor-driven sliding of antiparallel filaments, and the motor heads stall before reaching the filament plus ends (**Figure 2A1**). Filaments cannot be pushed apart, and hence cannot be reorganized into an aster. As a result, filaments remain crosslinked without significant clustering of plus ends. Increasing the sphere diameter to $D = 2L$ relaxes the spatial constraint on filament sliding, as crosslinking motors are now able to minimize antiparallel overlaps (**Figure 2A2**). However, the sphere is not large enough for a full aster to form if motors have non-zero rest length. The condensates in this case are half asters, similar to those seen experimentally [20]. For a sphere of diameter $D = 3L$, a full aster can form (**Figure 2A3**, **Supplementary Movie S2**).

Cylindrical confinement can drive filament alignment along the cylinder axis. **Figure 2B** shows results from simulations of $N = 1{,}600$ filaments at a packing fraction of $\phi = 0.08$ with $\tilde{N}_c = 3$ crosslinking motors. Here, the cylinder length is decreased as the cylinder diameter is increased in order to keep the system volume fixed at $V \approx 2.6$ μm^3. For $D = L$, we observe the formation of polarity-sorted bilayers (**Figure 2B1**, **Supplementary Movie S3**). Inside the bilayer, filament plus ends are held by a core of crosslinking motors in the center, and filaments have near perfect alignment along the axis of the confining cylinder. Increasing the cylinder diameter to $D = 2L$ allows condensed filaments to reorient and self-organize into a haystack-like asymmetric aster (**Figure 2B2**). This asymmetric aster retains some degree of orientational order relative to a full symmetric aster, as the preferred filament orientation is along the cylinder axis. For the case of a wide cylinder of diameter $D = 3L$ (**Figure 2B3**), crosslinking in the system leads to a filaments self-organizing into a single bottle brush-like aster state. This bottle brush-like aster is characterized by half asters at each end of the condensate. In the body of the condensate, filaments point radially in towards the cylindrical axis.

One-dimensional spatial constraints are modeled by confining the system between two hard planar surfaces. The degree of confinement is controlled by changing the separation H between the two surfaces. We investigate $N = 1{,}600$ filaments at a packing fraction of $\phi = 0.08$ with $\tilde{N}_c = 3$ crosslinking motors. In this case, the surface width is decreased as the surface separation is increased to keep the system volume fixed at $V \approx 2.6$ μm^3. In simulations with small surface separation $H = L$, filaments condense into flattened asters (**Figure 2C1**, **Supplementary Movie S4**). Filament condensates are surrounded by filaments in a vapor state containing few, if any, crosslinking motors. Inside the condensate, filaments are oriented in planes parallel to the confining surfaces. A core of crosslinking motors with a hollow center holds the filaments together. More symmetric aster morpohologies are recovered upon increasing the surface

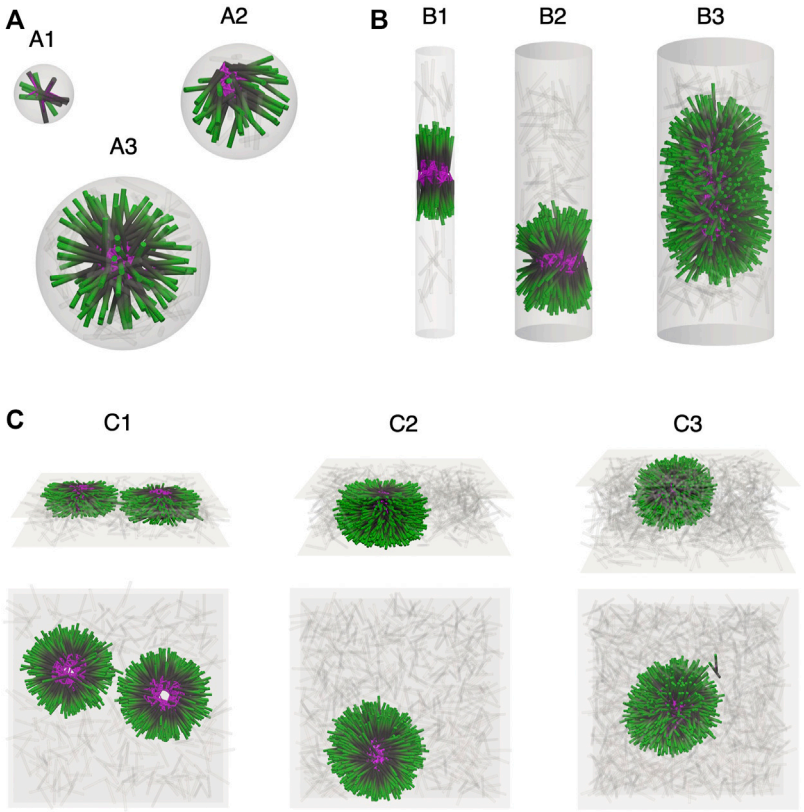

FIGURE 2 | Confinement lengthscale alters filament self-organization and steady-state morphology. Simulation snapshots showing filaments (minus end green, plus end black) of length L and end-pausing crosslinking motors (pink). Filaments in the vapor have been grayed out. **(A)** Spherical confinement in a sphere of varying diameter D. **(A1)** $D = L$. Small spherical boundary inhibits extensile force generation of the motor proteins and no tip accumulation is observed. **(A2)** $D = 2L$. The confining sphere is just large enough to allow for extensile stress generation, and crosslinking motor proteins accumulate at filament plus ends to form a half aster whose core is visible at the edge of the sphere. **(A3)** $D = 3L$. Filaments self-assemble into a symmetric aster centered in the confining sphere. **(B)** Cylindrical confinement of 1,600 filaments and 4,800 crosslinking motors in cylinders of varying diameter D. Snapshots show a 2 μm long section of the simulation cylinder. **(B1)** $D = L$. Filaments form polarity-sorted bilayers, each one held together by a core of crosslinking motors. **(B2)** $D = 2L$. An asymmetric aster showing a degree of orientational alignment of microtubules along the axis of the cylinder. **(B3)** $D = 3L$. A bottle-brush-like aster with an elongated core of crosslinking motors. Filaments point radially in towards the surface of the crosslinker core. **(C)** Planar confinement of 1,600 filaments and 4,800 crosslinking motor proteins between two surfaces with separation H. **(C1,C2)** $H = L$ and $H = 2L$. Flattened asters with a hollow filament core. **(C3)** $H = 3L$. The surface separation is large enough to accommodate a full, albeit slightly elongated, aster.

separation to $H = 2L$ and $H = 3L$ (**Figures 2C2,C3**). In the $H = 3L$ case, we see that the aster formed is slightly elongated, similar to that observed in the unconfined system (**Figure 1B**).

3.3 Ring-Like Asters Under Planar Confinement

Under planar confinement with surface separation $H = L$ and system volume $V \approx 5.3\,\mu m^3$, 1,600 filaments with packing fraction $\phi = 0.04$ condense into flattened asters in the presence of end-pausing crosslinking motors. The observed morphologies depend on the crosslinking motor number ratio $\tilde{N}_c = N_c/N$. At low crosslinker number, $\tilde{N}_c \in [1, 2, 3]$, plus-end association leads to the formation of multiple condensates (**Figure 3A**, **Supplementary Movie S5**). Both the aster size and the number of filaments in each aster are observed to increase with increasing $\tilde{N}_c$. At $\tilde{N}_c = 4$, the system self-organizes to form a single ring-like condensate (**Figure 3A**, **Supplementary Movie S6**). A novel feature of this ring-like aster is a hollow core free from both filaments and crosslinking motors. Crosslinking motors in the ring-like aster form a torus that holds filament plus ends. The radial distribution function $g(r)$ of filament plus ends sheds light on the local structure of the condensates (**Figure 3B**). A first peak at 25 nm, equal to the filament diameter, is evidence of steric exclusion and the close packing of filaments. A secondary peak at 78 nm, equal to the sum of filament diameter and the crosslinker rest length of 53 nm, arises from pairs of crosslinked filaments. Attractive forces, mediated by crosslinking motors, hold the aster together while steric interactions between filaments attempt to break up the aster. As filament number within the aster increases, a morphology change into a hollow and wider core is needed to accomodate the additional filaments within the aster. In geometric terms, a larger core of crosslinking motors leads to a larger core surface area. A larger surface area can host more filaments.

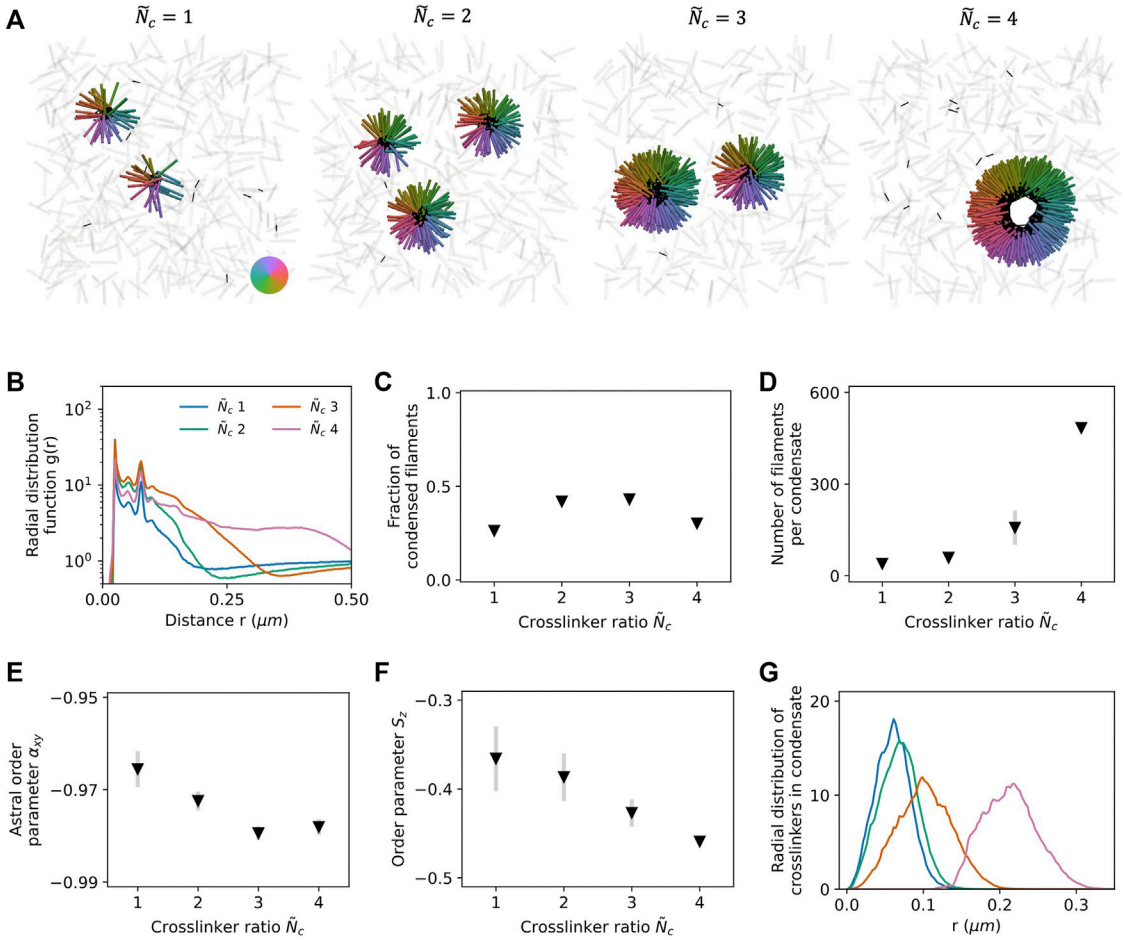

FIGURE 3 | Filaments and end-pausing crosslinking motor proteins self-assemble into flower-like and ring-like asters when confined between two planar surfaces with separation $H = L$. **(A)** Simulation snapshots for varying crosslinker number ratio $\tilde{N}_c = N_c/N$. End-pausing crosslinking motors (black) bind and walk on filaments (colored according to their *XY* orientation), before pausing at the filament plus end. Condensate morphology changes from flower-like ($\tilde{N}_c = 1, 2, 3$) to ring-like ($\tilde{N}_c = 4$). **(B)** Radial distribution function $g(r)$ computed for filament plus ends. The first peak at 25 nm, equal to the filament diameter, is due to steric exclusion between filament pairs. A second peak at 78 nm, the sum of filament diameter and crosslinking motor rest length, arises from crosslinked filament pairs. As $\tilde{N}_c$ increases, the size of the condensate increases, as evidenced by a widening of $g(r)$. **(C)** Fraction of condensed filaments increases to 0.45, before decreasing to 0.3 for $\tilde{N}_c = 4$. This dip in condensed fraction is due to the presence of a single aster, as opposed to multiple. **(D)** As $\tilde{N}_c$ increases, the number of filaments per condensate increases non-linearly. This is determined by the number of crosslinking motors per condensate. **(E)** The astral order parameter α_{xy} is negative for all condensates, indicating that the filament orientations in the *XY* plane tend to point toward the center of the condensate. The increase in the absolute value of α_{xy} with increasing $\tilde{N}_c$ is evidence for an increase in radial symmetry. **(F)** Scalar order parameter S_z of the condensed filaments decreases with increasing $\tilde{N}_c$, indicating an increase in alignment in the *XY* plane. **(G)** Radial distribution of crosslinking motors, measured relative to the center of the condensate. With increasing $\tilde{N}_c$, the crosslinker core widens and becomes hollow for $\tilde{N}_c = 4$. Note: C-F show mean values averaged over 10 s of a single simulation and error bars show standard deviation. Where not visible, errors are too small.

Using Gaussian mixture models, we cluster filaments and identify the filament populations belonging to the condensed and vapor states (**Supplementary Material**). The fraction of condensed filaments increases with $\tilde{N}_c$ to 0.45 before decreasing to 0.3 for $\tilde{N}_c = 4$ (**Figure 3C**). There are two explanations for this behavior. Since the crosslinking motors act as a condensing agent, increasing their number enables a larger number of filaments to become condensed. Therefore, as expected, the fraction of condensed filaments increases initially. Secondly, the reconfiguration of filaments upon coalescence leads to an ejection of filaments from the aster, thereby decreasing the number of condensed filaments. As aster size increases, filaments get more packed and consequently experience larger steric forces. This means that the attractive force per filament must increase in order to keep the aster together. Thus, a larger aster would require a larger number of crosslinkers per filament (**Supplementary Figure S2**) The initial increase in condensed fraction is caused by an increase in the number of crosslinking motors, which mediate aster formation. These asters coalesce over time, observed in our simulations, but may take a long time to coalesce into a single aster. The reduction in condensed fraction at $\tilde{N}_c = 4$ is related to the presence of a single aster, as opposed to multiple. Over time, we expect the asters in $\tilde{N}_c \in [\ 1,\ 2,\ 3]$ to coalesce into a single aster and the trend in condensed fraction to become monotonic. Condensate size, defined as the number of filaments per condensate, increases non-linearly with increasing $\tilde{N}_c$

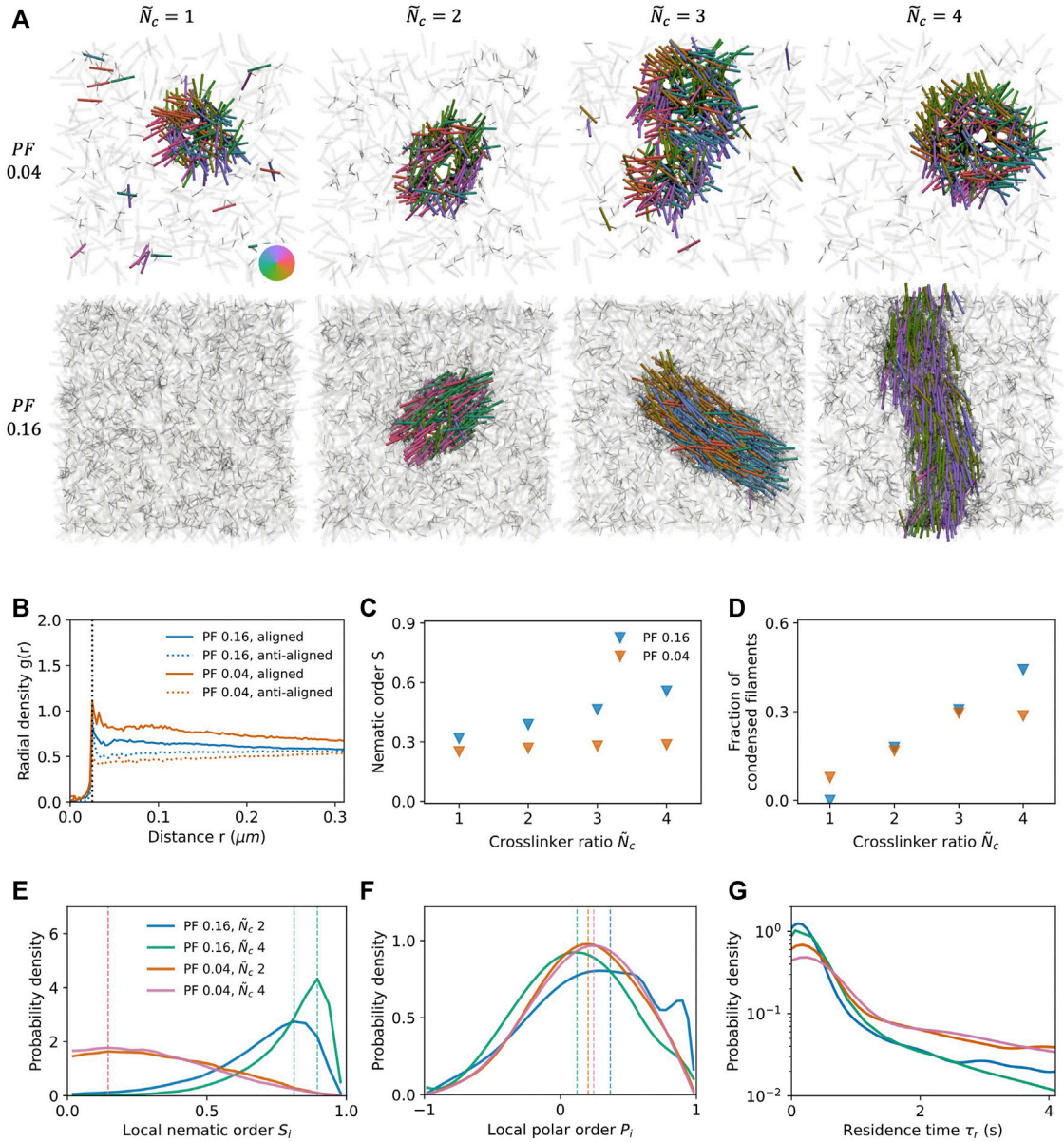

FIGURE 4 | Condensate formation in the presence of non-end-pausing crosslinking motor proteins under planar confinement with surface separation $H = L$. **(A)** Simulation snapshots at packing fraction $\phi = 0.04$ (top row) and 0.16 (bottom row) and varying crosslinker number ratio $\tilde{N}_c$. Crosslinking motors (black) bind and walk on filaments (colored according to their *XY* orientation) leading to extensile stress generation due to antiparallel sliding of anti-aligned filament pairs. At $\phi = 0.04$, motor activity leads to formation of condensates with low orientational order. At $\phi = 0.16$, no condensation is observed for $\tilde{N}_c = 1$, but increasing $\tilde{N}_c$ leads to condensation into bundles of increasing length and with a high degree of orientational order. **(B)** Center-of-mass radial distribution functions $g(r)$ for aligned and anti-aligned filaments. For both $\phi = 0.04$ (orange) and 0.16 (blue), the density of aligned filaments (solid lines) is greater than the density of anti-aligned filaments (dotted lines) for small pair separations ($r < 0.3$ μm), evidence for polarity sorting. **(C)** The global nematic order parameter S for the system is independent of $\tilde{N}_c$ for $\phi = 0.04$ but increases linearly with $\tilde{N}_c$ for $\phi = 0.16$. **(D)** The fraction of condensed filaments increases linearly with $\tilde{N}_c$ for both values of ϕ. However, for $\phi = 0.04$, the condensed fraction plateaus at ~ 0.3. **(E)** Probability density of the local nematic order parameter S_i within the condensate. For $\phi = 0.16$, condensed filaments have a high degree of local orientational order, evidenced by peaks at values greater than 0.8. **(F)** Probability density of the local polar order parameter P_i for all condensed filaments i. The presence of peaks in the density at positive values of P_i is evidence of polarity sorting. **(G)** Residence time τ_R for filaments within condensates. Filaments experience random directed motion in condensates with low ϕ and low orientational order, which leads to an increased residence time. For $\phi = 0.16$, filaments experience coherent directed motion which is more efficient at ejecting them from the condensate. Note: C-D show mean values averaged over 10 s of a single simulation and error bars show standard deviation. Where not visible, errors are too small.

(**Figure 3D**). We expect this to change with time for $\tilde{N}_c \in [1, 2, 3]$ as asters coalesce and get bigger, and the total number of asters decreases.

Radial symmetry of the condensate is quantified by defining an astral order parameter $\alpha = \langle \hat{r} \cdot \hat{u} \rangle$ where $\hat{u}$ is the filament orientation vector (oriented from the minus to the plus end), $\hat{r}$ is a radial director from the condensate center, and the angle brackets denote an ensemble average (**Supplementary Material**). Condensates with filaments oriented inward have $\alpha < 0$ while condensates with filaments oriented outward have $\alpha > 0$. When $\alpha = 0$, filaments have no inward or outward orientational preference. For planar-confined systems, the astral order parameter in XY, α_{xy}, is negative and increases in absolute value with increasing $\tilde{N}_c$, indicating that an increase in the number of filaments in the condensate is correlated with an increase in the astral order parameter (**Figure 3E**). Flattening of the condensate can be quantified using a scalar order parameter, $S_z = \frac{1}{2}\langle 3\cos^2\theta - 1\rangle$, where θ is the filament inclination angle measured from the + z-axis. In the limit in which all condensed filaments are aligned in the XY plane ($\theta = \pi/2$), $\cos\theta = 0$, and $S_z = -\frac{1}{2}$. Increasing $\tilde{N}_c$ leads to a decrease in S_z, indicating increased alignment in the XY plane (**Figure 3F**). To quantify the structural change from a flower-like aster to a ring-like aster, we look at the crosslinker core of the condensates. Measuring the radial density of crosslinkers relative to the condensate center, we find that the distribution resembles a Gaussian distribution (**Figure 3G**). Increasing $\tilde{N}_c$ from one to four leads to both a widening of the distribution and a shift in the mean value from ~0.05 μm to ~0.2 μm. The correlation hole in the $\tilde{N}_c = 4$ distribution at distances $r < 0.125$ μm indicates that the inner diameter of the core is roughly equal to the length of a single filament.

3.4 Polarity Sorted Condensates Formed by Non-End-Pausing Motors

Non-end-pausing crosslinking motors, including certain kinesins, do not exhibit tip accumulation on filaments. Instead of pausing upon reaching the filament plus end, both motor heads continue to walk and fall off of the filament. Consequently, the system is more active, and the kinetic pathways for system evolution are different than those in the case of end-pausing crosslinking motors [2, 3, 5]. Crosslinking and antiparallel sliding of anti-aligned filaments leads to extensile stress generation on the microscopic scale, and emergence of local order on the mesoscopic scale. Here, we study the effect of filament packing fraction ϕ and crosslinker number ratio $\tilde{N}_c$ on the structure of condensates in systems with non-end-pausing motors. We investigate this for planar-confined systems with 1,600 filaments and surface separation $H = L$. The system volume for $\phi = 0.04$ and 0.16 is fixed at $V_f = 5.2$ and 1.3 μm^3 respectively.

For a low filament packing fraction of $\phi = 0.04$, filaments condense into orientationally-disordered clusters (**Figure 4A** top row, **Supplementary Movie S7**). Increasing $\tilde{N}_c$ increases cluster size, but does not lead to emergence of any visible orientational order. At a high filament packing fraction of $\phi = 0.16$, the system transitions from a pure vapor state at $\tilde{N}_c = 1$ to exhibiting a coexistence of vapor and bundle-like condensed state for $\tilde{N}_c > 1$ (**Figure 4A** bottom row, **Supplementary Movie S8,S9**). The bundle size increases with $\tilde{N}_c$, eventually leading to a bundle spanning the length of the entire system at $\tilde{N}_c = 4$. One phenomenon evident in these simulations is that of polarity sorting. A result of sliding anti-aligned filaments apart is that filaments are more likely to be in an aligned state rather than an anti-aligned state. The radial distribution function $g(r)$ for filament centers of mass (**Figure 4B**) shows that neighboring pairs of filaments are more likely to be aligned (solid curves) than anti-aligned (dotted curves). Furthermore, we find that the scalar order parameter S, a measure of the global orientational order, does not depend on $\tilde{N}_c$ for a packing fraction of 0.04 and increases linearly with $\tilde{N}_c$ for a packing fraction of $\phi = 0.16$ (**Supplementary Material**). This is a direct result of increasing condensate size, with larger condensates displaying a higher degree of orientational order.

We next measure the fraction of filaments in the condensed state as a function of $\tilde{N}_c$ (**Figure 4D**). For the low packing fraction systems, the condensed fraction increases and plateaus at ~ 0.3. By contrast, in the high packing fraction systems, the fraction of filaments in condensates increases linearly from 0 to 0.45. It is clear from the simulation snapshots (**Figure 4A**) that the degree of local orientational order is significantly lower in the low packing fraction systems (top row) than in the high packing fraction systems (bottom row). Computing the local nematic order S_i for all condensed filaments i, we find that the distribution for the two cases is very different (**Figure 4E**, **Supplementary Material**). The probability distribution of S_i has a peak (blue and green dashed line) at values > 0.8 for $\phi = 0.16$, indicating the presence of high local orientational order within condensates. For the low packing fraction of $\phi = 0.04$, this distribution peaks ~ 0.2 (orange and pink dashed line).

A second measure of orientational order is the local polar parameter P_i, which is a quantitative measure of the local polar alignment of a given filament i (**Figure 4F**, **Supplementary Material**). A system with a random mixture of aligned and anti-aligned filaments (as in a conventional nematic) would have $P_i = 0$, while a system where all filaments are perfectly aligned/anti-aligned would have $P_i = \pm 1$. Polarity sorting in the system leads to probablility distributions with peaks at positive values of P_i (dashed lines). The distributions for $\phi = 0.04$ are very similar, while for $\phi = 0.16$ there are similarities and significant differences between the distributions for $\tilde{N}_c = 2$ and $\tilde{N}_c = 4$ (blue and green curve). The peak values for $\tilde{N}_c = 2$ and $\tilde{N}_c = 4$ are located at ~ 0.4 and ~ 0.1. In the case of $\tilde{N}_c = 4$, the space-spanning bundle depicts a case where polarity sorting is less efficient. Filaments in the center of the bundle continuously get transported and it is difficult for them to find polarity sorted domains. Both of these cases also contain a small second peak near $P_i \sim 0.9$, showing the presence of a small population of highly ordered filaments. This peak is more evident for $\tilde{N}_c = 2$ than for $\tilde{N}_c = 4$ in **Figure 4F**.

Lastly, to quantify coherence, we measure the residence time τ_R of filaments in the condensed state (**Figure 4G**). In the low packing fraction systems, condensed filaments experience random directed motion within the orientationally-disordered

condensate and consequently remain in the condensate for a relatively longer time. By contrast, the high degree of orientational order in the high packing fraction systems leads to coherent directed motion of filaments within the condensate, so that they can more easily be ejected from the condensate.

4 DISCUSSION

Microbutule self-assembly is sensitive to spatial confinement. *In vivo*, there is interplay between cell shape and microtubule self-assembly, where cell shape affects microtubule orientational order [15, 16]. *In vitro*, assemblies of microtubules and end-pausing crosslinking motors form asters that are able to sense their surroundings and use that information for positioning [18]. Moreover, aster formation is perturbed in suspensions of Xenopus egg extract confined to spherical oil droplets, where microtubules self-assemble into cortical and half-aster states when the droplet size is small [20, 21]. Here, we find that fixed-length filaments assemble into half asters when the confinement diameter of the sphere is on the order of twice the length of a single filament. For smaller diameters, asters cannot form. For successful aster assembly, anti-aligned crosslinked filaments need to slide apart. This kinetic pathway requires that the diameter of the confining sphere be at least twice as long as the length of a single filament. When the confining diameter is three times the filament length, pairs of anti-aligned filaments remain unimpeded in both sliding apart and pivoting to form full asters.

In vitro, filament behavior and self-assembly in the presence of molecular motors is often studied in the presence of depleting agents [29]. Depleting agents, like PEG and methylcellulose, push filaments to the surface forming a thin layer, and increase the potential for filament interaction by forcing the filaments to lie in a single two-dimensional plane [30]. The use of a depletion agent effectively introduces a depletion interaction, which may be modeled in terms of an additional degree of spatial confinement. Here, we simulate filaments and crosslinking motor proteins confined between two planar surfaces. Under planar confinement, when the plate separation is equal to filament length, we find that systems of filaments and end-pausing crosslinking motors form flattened asters. Filaments in this condensed fraction have a tendency to align in the confinement plane, shown by a negative value for S_z. As the number of crosslinking motors is increased, we observe that the flattened aster dilates and becomes ring-like, with a hollow core that is free from both filaments and crosslinking motors. In experiments with Xenopus egg cytosol, taxol-stabilized microtubules self-assemble into both flattened ring-like and bilayer-like structures [31]. Simulations with higher number of filaments, and crosslinking motor proteins may yield assymetric condensates that resemble bilayers.

The coexistence of condensed and vapor phases in which most of the crosslinking motors accumulate in the condensed fraction bears an intriguing resemblance to amphiphile-based micelles. Instead of repulsive hydrophobic interaction due to chemical differences between head and tail groups, however, active condensates form due to localized crosslinker-mediated attractive interactions between filament plus ends. As a result, filament plus ends condense, while filament minus ends sterically repel each other, leading to micelle-like aster morphologies.

In the case of non-end-pausing crosslinking motors, the attractive interaction between filaments is no longer localized and is instead distributed along the length of the filament. Here, as expected, we find that filaments associate together into clusters or bundles. At low filament packing fraction, condensed clusters lack orientational order. Filaments prefer an isotropic distribution in this regime, and the addition of crosslinking motors introduces motility without affecting the local orientational order. Filaments form disordered clusters, and the variety of filament orientations mean that crosslinking motors have small overall displacement. This, in turn, allows crosslinking motors to aggregate together, enabling condensate formation. While the number of condensed filaments increases, the lack of orientational order persists when the crosslinker number ratio $\tilde{N}_c$ is increased from 1 to 4. Increasing the filament packing fraction to $\phi = 0.16$ yields orientationally-ordered bundles above a critical number of crosslinking motors (between $\tilde{N}_c = 1$ and $\tilde{N}_c = 2$). In high packing fraction equilibrium systems, filaments are more likely to be locally ordered [32]. We observe similar behavior in these non-equilibrium systems. At $\tilde{N}_c = 1$, filaments form locally-ordered polarity-sorted domains. The increased local polar order means that crosslinking motors encounter and slide anti-aligned filaments less often, and in turn they are able to be highly mobile. In comparison, the disordered clusters for $\phi = 0.04$ act as sinks for crosslinking motors. At $\tilde{N}_c = 1$, while we observe polarity-sorted domains, there are no crosslinker-dense condensed regions. There may be a critical crosslinker concentration that is required for the formation of nematic bundles. At $\tilde{N}_c \geq 2$, the crosslinker concentration exceeds the critical threshold as evidenced by the presence of nematic bundles.

The orientationally-ordered bundles for $\phi = 0.16$ show an increase in aspect ratio with increasing $\tilde{N}_c$ Bundle length increases and width remains constant ($W \sim 3L$). While there has been considerable work describing condensate shape in equilibrium systems (such as nematic droplets), the same is not true for non-equilibrium systems [33, 34]. There are two kinetic pathways for bundle evolution, with filaments entering the bundle laterally and leaving the bundle longitudinally. There may be a balance between these two pathways, leading to a characteristic width of $W \sim 3L$. Measurement of the number of crosslinking motors per filament for the condensed state (**Supplementary Figure S2**), shows that condensed filaments contain ~ 7.0 crosslinking motors for $2 \leq \tilde{N}_c \leq 4$. It is possible that this determines filament transport through the condensate, which may affect the characteristic bundle width. Both low and high packing fraction systems exhibit polarity sorted domains, indicated by a positive-valued peak in the local polar order distribution. This is a result of increased local packing fraction within the condensate. As crosslinking

motors mediate filament condensation, the local packing fraction of condensed filaments increases, driving a transition into an active nematic state.

In summary, here we describe active condensate morphology in filament and crosslinking motor assemblies in a variety of geometries. Confinement can alter the self-organization of such assemblies by inhibiting certain kinetic pathways, in the case of spherical confinement. We find that self-assembled filament structures in the presence of end-pausing crosslinking motors are strongly dependent in their morphology to the type and degree of confinement. Flattened asters under planar confinement transition to a unique hollow and ring-like state. Planar-confined filament systems with non-end-pausing motors transition to a highly ordered and polarity-sorted nematic state upon increasing the filament packing fraction. The interplay between activity and confinement has significant implications for biological functionality. Our work shows the importance of how confinement can modify the morphology of active condensates.

DATA AVAILABILITY STATEMENT

The original contributions presented in the study are included in the article/**Supplementary Material**, further inquiries can be directed to the corresponding author.

AUTHOR CONTRIBUTIONS

SA performed and analyzed the simulations, and wrote the manuscript. AL, MG, and MB edited the manuscript. WY and AL created the aLENS software used in these simulations. MS, MG, and MB supervised the project.

FUNDING

SA, AL, MG, and MB acknowledge support from NSF grants DMS-1821305, DMR-1420736, and NIH grant RGM124371A. MS acknowledges support from NSF grants DMR-2004469 and CMMI-1762506. This work utilized resources from the University of Colorado Boulder Research Computing Group, which is supported by the National Science Foundation (awards ACI-1532235 and ACI-1532236), the University of Colorado Boulder, and Colorado State University.

SUPPLEMENTARY MATERIAL

The Supplementary Material for this article can be found online at: https://www.frontiersin.org/articles/10.3389/fphy.2022.897255/full#supplementary-material

REFERENCES

1. Foster PJ, Fürthauer S, Shelley MJ, Needleman DJ. Active Contraction of Microtubule Networks. *Elife* (2015) 4:e10837. doi:10.7554/eLife.10837
2. Gompper G, Winkler RG, Speck T, Solon A, Nardini C, Peruani F, et al. The 2020 Motile Active Matter Roadmap. *J Phys Condens Matter* (2020) 32:193001. doi:10.1088/1361-648x/ab6348
3. Moore JM, Thompson TN, Glaser MA, Betterton MD. Collective Motion of Driven Semiflexible Filaments Tuned by Soft Repulsion and Stiffness. *Soft Matter* (2020) 16:9436–42. doi:10.1039/d0sm01036g
4. Bricard A, Caussin JB, Desreumaux N, Dauchot O, Bartolo D. Emergence of Macroscopic Directed Motion in Populations of Motile Colloids. *Nature* (2013) 503:95–8. doi:10.1038/nature12673
5. Roostalu J, Rickman J, Thomas C, Nédélec F, Surrey T. Determinants of Polar versus Nematic Organization in Networks of Dynamic Microtubules and Mitotic Motors. *Cell* (2018) 175:796–808. doi:10.1016/j.cell.2018.09.029
6. Redner GS, Hagan MF, Baskaran A. Structure and Dynamics of a Phase-Separating Active Colloidal Fluid. *Phys Rev Lett* (2013) 110:055701. doi:10.1103/PhysRevLett.110.055701
7. Ndlec FJ, Surrey T, Maggs AC, Leibler S. Self-organization of Microtubules and Motors. *Nature* (1997) 389:305–8. doi:10.1038/38532
8. Theurkauff I, Cottin-Bizonne C, Palacci J, Ybert C, Bocquet L. Dynamic Clustering in Active Colloidal Suspensions with Chemical Signaling. *Phys Rev Lett* (2012) 108:268303. doi:10.1103/physrevlett.108.268303
9. Palacci J, Sacanna S, Steinberg AP, Pine DJ, Chaikin PM. Living Crystals of Light-Activated Colloidal Surfers. *Science* (2013) 339:936–40. doi:10.1126/science.1230020
10. Fily Y, Marchetti MC. Athermal Phase Separation of Self-Propelled Particles with No Alignment. *Phys Rev Lett* (2012) 108:235702. doi:10.1103/physrevlett.108.235702
11. Lemma B, Mitchell NP, Subramanian R, Needleman DJ, Dogic Z. Active Microphase Separation in Mixtures of Microtubules and Tip-Accumulating Molecular Motors. *arXiv preprint arXiv:2107.12281* (2021).
12. Surrey T, Ne´de´lec F, Leibler S, Karsenti E. Physical Properties Determining Self-Organization of Motors and Microtubules. *Science* (2001) 292:1167–71. doi:10.1126/science.1059758
13. Lombardo D, Kiselev MA, Magazù S, Calandra P. Amphiphiles Self-Assembly: Basic Concepts and Future Perspectives of Supramolecular Approaches. *Adv Condensed Matter Phys* (2015) 2015. doi:10.1155/2015/151683
14. Israelachvili JN, Mitchell DJ, Ninham BW. Theory of Self-Assembly of Hydrocarbon Amphiphiles into Micelles and Bilayers. *J Chem Soc Faraday Trans 2* (1976) 72:1525–68. doi:10.1039/f29767201525
15. Carazo-Salas RE, Nurse P. Self-organization of Interphase Microtubule Arrays in Fission Yeast. *Nat Cel Biol* (2006) 8:1102–7. doi:10.1038/ncb1479
16. Terenna CR, Makushok T, Velve-Casquillas G, Baigl D, Chen Y, Bornens M, et al. Physical Mechanisms Redirecting Cell Polarity and Cell Shape in Fission Yeast. *Curr Biol* (2008) 18:1748–53. doi:10.1016/j.cub.2008.09.047
17. Holy TE, Dogterom M, Yurke B, Leibler S. Assembly and Positioning of Microtubule Asters in Microfabricated chambers. *Proc Natl Acad Sci U.S.A* (1997) 94:6228–31. doi:10.1073/pnas.94.12.6228
18. Sulerud T, Sami AB, Li G, Kloxin A, Oakey J, Gatlin J. Microtubule-dependent Pushing Forces Contribute to Long-Distance Aster Movement and Centration in xenopus Laevis Egg Extracts. *MBoC* (2020) 31:2791–802. doi:10.1091/mbc.e20-01-0088
19. Islam MS, Kuribayashi-Shigetomi K, Kabir AMR, Inoue D, Sada K, Kakugo A. Role of Confinement in the Active Self-Organization of Kinesin-Driven Microtubules. *Sensors Actuators B: Chem* (2017) 247:53–60. doi:10.1016/j.snb.2017.03.006
20. Pinot M, Chesnel F, Kubiak JZ, Arnal I, Nedelec FJ, Gueroui Z. Effects of Confinement on the Self-Organization of Microtubules and Motors. *Curr Biol* (2009) 19:954–60. doi:10.1016/j.cub.2009.04.027
21. Gai Y, Setru S, Gouveia B, Stone H, Petry S. Self-organization of Microtubules in Cell-Sized Droplets. *Bull Am Phys Soc* (2019) 64.
22. Suzuki K, Miyazaki M, Takagi J, Itabashi T, Ishiwata Si. Spatial Confinement of Active Microtubule Networks Induces Large-Scale Rotational Cytoplasmic Flow. *Proc Natl Acad Sci U.S.A* (2017) 114:2922–7. doi:10.1073/pnas.1616001114

23. Fan Y, Wu KT, Aghvami SA, Fraden S, Breuer KS. Effects of Confinement on the Dynamics and Correlation Scales in Kinesin-Microtubule Active Fluids. *Phys Rev E* (2021) 104:034601. doi:10.1103/PhysRevE.104.034601
24. Wu KT, Hishamunda JB, Chen DT, DeCamp SJ, Chang YW, Fernández-Nieves A, et al. Transition from Turbulent to Coherent Flows in Confined Three-Dimensional Active Fluids. *Science* (2017) 355:eaal1979. doi:10.1126/science.aal1979
25. Yan W, Ansari S, Lamson A, Glaser MA, Betterton M, Shelley MJ. Alens: towards the Cellular-Scale Simulation of Motor-Driven Cytoskeletal Assemblies. *arXiv preprint arXiv:2109.08206* (2021).
26. Gao T, Blackwell R, Glaser MA, Betterton MD, Shelley MJ. Multiscale Modeling and Simulation of Microtubule-Motor-Protein Assemblies. *Phys Rev E Stat Nonlin Soft Matter Phys* (2015) 92:062709. doi:10.1103/PhysRevE.92.062709
27. Nedelec F, Foethke D. Collective Langevin Dynamics of Flexible Cytoskeletal Fibers. *New J Phys* (2007) 9:427. doi:10.1088/1367-2630/9/11/427
28. Heyes DM, Melrose JR. Brownian Dynamics Simulations of Model Hard-Sphere Suspensions. *J non-newtonian Fluid Mech* (1993) 46:1–28. doi:10.1016/0377-0257(93)80001-r
29. Weirich KL, Dasbiswas K, Witten TA, Vaikuntanathan S, Gardel ML. Self-organizing Motors divide Active Liquid Droplets. *Proc Natl Acad Sci U.S.A* (2019) 116:11125–30. doi:10.1073/pnas.1814854116
30. Saito A, Farhana TI, Kabir AMR, Inoue D, Konagaya A, Sada K, et al. Understanding the Emergence of Collective Motion of Microtubules Driven by Kinesins: Role of Concentration of Microtubules and Depletion Force. *RSC Adv* (2017) 7:13191–7. doi:10.1039/c6ra27449h
31. Mitchison TJ, Nguyen P, Coughlin M, Groen AC. Self-organization of Stabilized Microtubules by Both Spindle and Midzone Mechanisms inXenopusegg Cytosol. *MBoC* (2013) 24:1559–73. doi:10.1091/mbc.e12-12-0850
32. Bolhuis P, Frenkel D. Tracing the Phase Boundaries of Hard Spherocylinders. *J Chem Phys* (1997) 106:666–87. doi:10.1063/1.473404
33. Prinsen P, Van Der Schoot P. Shape and Director-Field Transformation of Tactoids. *Phys Rev E Stat Nonlin Soft Matter Phys* (2003) 68:021701. doi:10.1103/PhysRevE.68.021701
34. Weirich KL, Banerjee S, Dasbiswas K, Witten TA, Vaikuntanathan S, Gardel ML. Liquid Behavior of Cross-Linked Actin Bundles. *Proc Natl Acad Sci U.S.A* (2017) 114:2131–6. doi:10.1073/pnas.1616133114

Conflict of Interest: The authors declare that the research was conducted in the absence of any commercial or financial relationships that could be construed as a potential conflict of interest.

Publisher's Note: All claims expressed in this article are solely those of the authors and do not necessarily represent those of their affiliated organizations, or those of the publisher, the editors and the reviewers. Any product that may be evaluated in this article, or claim that may be made by its manufacturer, is not guaranteed or endorsed by the publisher.